PAPER

Check for updates

Low-temperature growth of high-conductivity graphene/copper structures: applications in energy-efficient graphene photodetectors

Yu-Jin Liu,[a] Yi-Hsiang Shih,[b] Peng-Chi Wang,[a] Yi-Cheng Huang,[a] Shu-Wei Wang [ID] *[acd] and Wei-Chen Tu [ID] *[abd]

This study demonstrates a simple and effective two-step strategy for synthesizing high-quality graphene on copper foils at a low growth temperature of 400 °C, significantly reducing the temperature required compared with conventional CVD methods. First, CO_2 laser pretreatment is applied to the copper substrate, which significantly improves surface smoothness and reduces surface oxides and particulates through localized heating. This process effectively lowers the nucleation density, thereby promoting the formation of larger graphene domains with fewer grain boundaries. Importantly, this approach addresses the common challenge of high defect density in low-temperature-synthesized graphene, enabling the production of films with excellent electrical and structural quality. The graphene/Cu hybrid structure achieves a 66.9% reduction in electrical resistance compared to pristine copper foil and demonstrates outstanding oxidation resistance. To demonstrate practical relevance, a photodetector fabricated using the low-temperature graphene exhibits a high responsivity of 666.95 mA W^{-1} and a detectivity of 2.32 × 10^{10} Jones under 5 V bias and 100 W m^{-2} illumination. Moreover, it maintains stable switching performance even at 0.1 V, highlighting its suitability for low-power optoelectronic and sensor applications.

1 Introduction

Graphene, composed of one layer of carbon atoms bonded by covalent bonds in an sp^2 hybridized orbital configuration, forms a flat honeycomb lattice. Each carbon atom is tightly connected to the three neighboring carbon atoms. Graphene exhibits unique linear optical properties due to its two-dimensional (2D) band structure. It absorbs approximately 2.3% of incident red light and 2.6% of green light per layer.[1] The electronic structure of graphene also allows for the absorption of a broad spectrum of light, ranging from ultraviolet to mid-infrared, and even extending to terahertz (THz) frequencies (corresponding to wavelengths from 30 μm to 3 mm).[2] Moreover, the high carrier mobility in graphene enables high-speed operation of optical sensors.[3] The fast response and compatibility with electronic circuits render graphene promising for applications in photodetectors. Due to its extremely high specific surface area (up to 2630 m^2 g^{-1}), graphene is often

proposed as a substitute for activated carbon in supercapacitors, making it particularly suitable for storing electrostatic charge with minimal performance degradation over long-term cycling.[4] Graphene is also widely used as a reinforcing material in coatings to improve wear resistance.[5,6] Prasai *et al.* finds that in sodium sulfate solution, the corrosion rate of copper covered with graphene is seven times lower than that of bare copper. When nickel is coated with graphene, its corrosion resistance even improves by 20 times.[7] Studies by Chen *et al.* demonstrate that coating copper and silicon surfaces with graphene effectively prevents oxidation, even after heating at 200 °C for up to 4 hours.[8] These findings highlight graphene's potential as a protective layer, significantly enhancing the corrosion and oxidation resistance of metals. Therefore, graphene films with good quality have multiple advantages when used in fabricating electronic and optoelectronic devices.

Among the various methods for preparing graphene, chemical vapor deposition (CVD) is the most effective technique for synthesizing large-area, high-quality graphene, making it a focus of attention for researchers. In 2008, Yu and colleagues were the first to use CVD to synthesize graphene on polycrystalline nickel foils at 1000 °C under ambient pressure, with methane as the carbon source.[9] Later, in 2009, De Arco *et al.* grew single-layer and multi-layer graphene at 800 °C by introducing 100 sccm of methane gas into the chamber.[10] The impact of growth temperature on graphene nucleation density and surface coverage was analyzed by Chaitoglou and Bertran

[a]*Department of Electrical Engineering, National Cheng Kung University, Tainan 701, Taiwan. E-mail: shuweiwang@gs.ncku.edu.tw*

[b]*Program on Nano-IC Engineering, National Cheng Kung University, Tainan 701, Taiwan. E-mail: wctu@gs.ncku.edu.tw*

[c]*Institute of Microelectronics, National Cheng Kung University, Tainan 701, Taiwan*

[d]*Program on Semiconductor Manufacturing Technology, Academy of Innovative Semiconductor and Sustainable Manufacturing, National Cheng Kung University, Tainan 701, Taiwan*

(970–1070 °C)[26] as well as Dapthon and Chaisitsak (650–950 °C).[27] Higher temperatures can increase the growth rate while reducing the nucleation density, producing high-quality monolayer graphene. Therefore, traditional CVD techniques typically require high temperatures (>800 °C) to deposit large-area, high-quality graphene on the surface of copper foils.[11–16] However, high growth temperatures significantly increase the cost and limit the application of graphene in flexible electronic devices and back-end-of-line (BEOL) semiconductor manufacturing processes because high thermal budgets can damage temperature-sensitive substrates or disrupt BEOL structures.[28,29] In addition, for optoelectronics, the incorporation of graphene can significantly enhance the device's conductivity. However, certain optoelectronic devices require graphene growth at low temperatures, typically below 600 °C. To overcome this challenge, plasma-enhanced chemical vapor deposition (PECVD) is employed, which not only lowers the growth temperature of graphene to about 400 °C but also increases its growth rate.[17–21] Our proposed PECVD process meets this requirement by producing high-quality graphene at 400 °C, making it suitable for BEOL-compatible and flexible optoelectronic applications. This low-temperature capability also makes PECVD a key technology for enabling the mass production and commercial deployment of graphene-based devices. (The PECVD growth mechanism of graphene is explained in SI).

Recent studies integrated continuous graphene sheets with microscale copper wires to enhance the electrical conductivity and oxidation resistance of graphene/copper composite structures.[22–24] At a low temperature of 400 °C, researchers successfully synthesized copper-graphene core–shell nanostructures using low-temperature PECVD.[25] The impermeable graphene shell encasing the copper core showed remarkable thermal oxidation and chemical stability. Moreover, the transparent conducting electrodes (TCEs) based on copper-graphene core–shell nanostructures exhibited excellent optical and electrical properties comparable to those of conventional indium tin oxide (ITO). These findings suggest that copper-graphene core–shell structures could serve as a promising alternative to traditional TCE materials in emerging optoelectronic devices such as flexible solar cells, displays, and touch panels.

This study primarily focuses on synthesizing high-quality graphene at a low temperature (400 °C) using PECVD. By using benzene as the carbon source and copper as the catalyst, we explore the effects of copper foil pretreatment (*i.e.*, using a CO_2 laser to smooth the copper foil) and growth parameters (*e.g.*, the temperature, the distance between the sample and the plasma source, and annealing) on the quality of graphene. Through the optimization of growth parameters, we reduce the defects of graphene film that usually occur in low-temperature growth, which implies not only a lower cost and energy consumption of graphene production but also a higher applicability in practical applications. Finally, we compare the electrical resistance of graphene/copper composites with pure copper sheets and evaluate the performance of this graphene optoelectronic system. The results confirm the successful development of graphene-based photodetectors with significant on-off response and low energy consumption characteristics, demonstrating great potential for advancing power-efficient sensing technology in the future.

# 2 Methods

2.1 Substrate pretreatment

The quality of graphene growth can be improved by controlling nucleation sites through substrate pretreatment. Less nucleation sites on the substrate surface will be more favorable for the growth of large-area single-crystal graphene films. In this work, a 25 μm-thick copper foil with a purity of ≥99.8% was used as the substrate. (More discussions about the substrate used for graphene growth are in SI). A universal laser systems CO_2 continuous laser was used for the pretreatment of substrates. The laser pretreatment primarily involves continuously irradiating the copper foil with a high-energy CO_2 laser, which removes surface particles on the copper foil and thus reduces nucleation sites. The effect of different laser powers on the substrate was also investigated.

2.2 The growth of graphene

Fig. 1a shows the inductively coupled plasma PECVD (ICP-PECVD) system used in this work. The carbon source gas (benzene, C_6H_6) is cracked by the plasma, forming a graphene layer on the treated copper foil surface, achieving uniform high-quality graphene growth. More discussions about the gases used for graphene growth are in SI.

In this work, we explored a variety of growth parameters (*e.g.*, temperatures, positions and gases in the chamber, and growth durations) to identify the best conditions for graphene growth. The experiment details determining these optimized conditions are shown in Results and discussion. A typical graphene growth procedure is described as follows. First, the copper foil substrate was placed in a quartz boat and inserted into the furnace tube of the PECVD system, with a distance of 10–25 cm between the sample and the plasma source. After sealing the chamber, a vacuum pump was used to evacuate the chamber to below 0.03 Torr. Then, 2000 sccm of Ar gas was introduced, raising the pressure to 650 Torr. The graphene growth was divided into multiple steps, as illustrated in Fig. 1b. Step 1 is the heating phase. We introduced 200 sccm of Ar gas to create an inert environment in the chamber and increased the furnace temperature to 400 °C. Step 2 is the surface cleaning phase. Once the temperature reached 400 °C, we stopped the Ar gas flow and introduced 150 sccm of H_2 gas for 60 minutes. The etching effect of H_2 gas removes surface oxides and can improve the uniformity of graphene. Step 3 is the growth phase. We introduced 75 sccm of Ar gas and 15 sccm of H_2 gas, and activated the RF plasma source at 300 W. The Ar gas transported the heated gaseous carbon source, benzene, at 82 °C into the quartz chamber, providing a 20 second growth time. Step 4 is the low-temperature annealing phase. We maintained the temperature at 400 °C for 30 minutes and turned off the H_2 gas and plasma while introducing a small amount of Ar gas at 75 sccm to prevent hole defects in the graphene due to excessive gas flow.
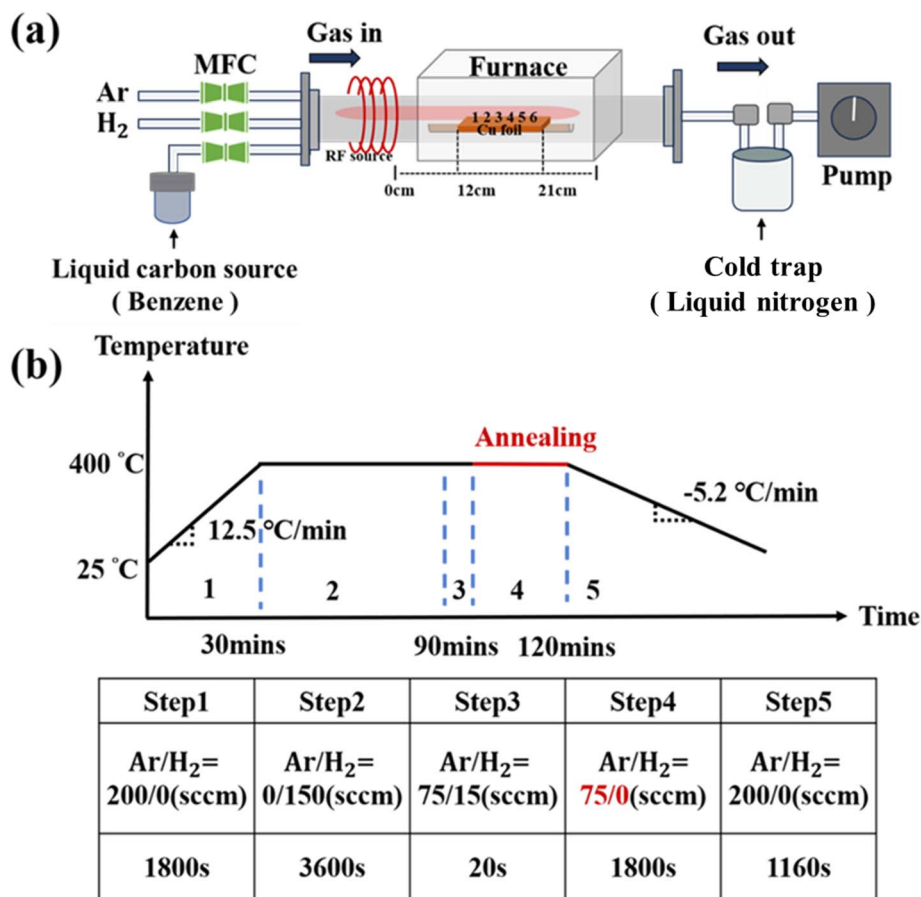
Fig. 1   The PECVD growth process. (a) The PECVD system used in this work. The CVD chamber has a 1-inch diameter quartz tube. A mass flow controller (MFC) regulates the flow rates of the carbon source, hydrogen, and argon. A high-vacuum pump controls the pressure in the chamber. The liquid nitrogen cold trap cools the carbon source to prevent the carbon source gas from damaging the pump. (b) The graphene growth process. The upper panel shows the temperature variation with respect to time, which can be divided into five steps. The lower panel shows the parameters (i.e., gas flow rates and the corresponding durations) at each step.

Step 5 is the cooling phase. We introduced 200 sccm of Ar gas. After 1160 seconds, the temperature dropped from 400 °C to 180 °C at a rate of 5.2 °C min^{-1}. The cooling rate should not be too fast, as it could induce thermal stress within the graphene film, leading to cracks and defects. The furnace was opened after the temperature reached 180 °C to allow it to cool to room temperature.

2.3   Graphene transfer and electrode fabrication

After the growth of graphene, we have to transfer the film from the copper foil onto a Si substrate for the subsequent device fabrication. The transfer process is a critical factor that affects the final quality of graphene. In this work, we used an improved approach that can reduce defects generated during the wet transfer process. Detailed transfer process is described in SI. Finally, a thermal evaporator was used to evaporate interdigitated silver electrodes. This interdigitated design can increase the active area of the photodetector, enhance light absorption efficiency, and shorten the migration path of photogenerated carriers. More details can be found in SI.

3   Results and discussion

3.1   Comparison of growth conditions for graphene/copper foil

The ratio of argon to hydrogen (Ar : H$_2$) is a crucial factor influencing the quality of graphene.[30,31] Argon not only serves to purge the CVD quartz tube, maintaining an inert environment to prevent oxidation of the copper foil but also helps introduce the vaporized liquid carbon source into the CVD chamber for graphene growth. The concentration of hydrogen also plays a critical role in the quality of graphene growth. An appropriate concentration of hydrogen can effectively etch away the amorphous carbon at the edges of the graphene, maintaining edge activity and promoting the formation of a continuous graphene film. However, if the hydrogen concentration is too high, it may over-etch the graphene surface, causing more defects in graphene. In the first experiment, graphene growth was conducted at 400 °C, at distances of 12 cm to 20 cm from the plasma source, while introducing Ar : H$_2$ = 75 : 15 (sccm). Under these conditions, the impact of growth times (ranging from 20 to 60 seconds) on graphene quality was investigated. The growth was
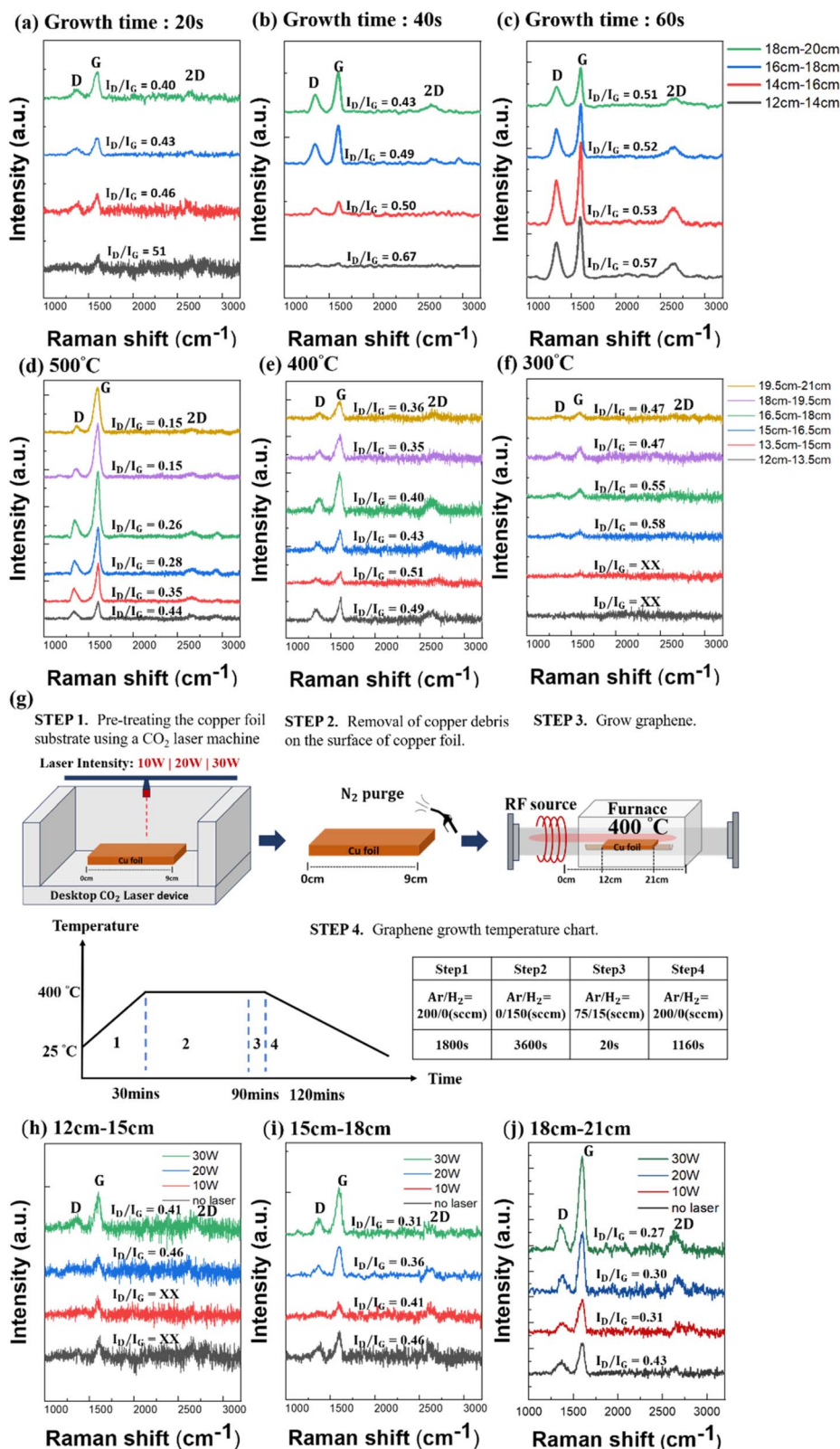
Fig. 2 Graphene growth with different conditions. (a–c) Raman spectra of graphene/copper foil with different growth times and at various growth distances. The growth times are (a) 20 seconds, (b) 40 seconds, and (c) 60 seconds. The distances to the plasma source are 12–14 cm (black), 14–16 cm (red), 16–18 cm (blue), and 18–20 cm (green). (d–f) Raman spectra of graphene/copper foil at different growth temperatures: (d) 500 °C, (e) 400 °C, and (f) 300 °C. The distance between the samples and the plasma source was divided into six groups, between 12 cm and 21 cm. (g) Laser pretreatment process (upper panel) and growth timetable (lower panel). (h–j) Raman spectra of graphene with and without the laser pretreatment at different growth distances: (h) 12–15 cm, (i) 15–18 cm, and (j) 18–21 cm. The green, blue, red, and black curves correspond to 30 W, 20 W, 10 W, and no laser treatment, respectively.

subdivided based on different growth durations, and the distance between the graphene and plasma source, as shown in Fig. 2a–c. The intensity ratio of the D peak (~1350 cm^{-1}) to the G peak (~1585 cm^{-1}) (I_D/I_G ratio) in the Raman spectrum gradually increases as the growth time increases, from 0.40 to 0.51, suggesting an increase in defect density. The possible reason is that the prolonged growth time leads to excessive carbon atom accumulation on the graphene surface, which increases internal stress and results in more structural defects such as single vacancies, multi-vacancies, and Stone–Wales (SW) defects.[32,33] Therefore, it is essential to control the growth time (~20 seconds) to avoid the formation of excessive defects in graphene.

As for the dependence on distance to the plasma source, four different distances (12–14 cm; 14–16 cm; 16–18 cm; 18–20 cm) were tested. It can be seen in Fig. 2a–c that, regardless of the growth time, the I_D/I_G value decreases as the distance from the plasma source increases, suggesting that the farther the distance, the better the quality of graphene. This is due to high-energy radicals and ions accelerated by the high electric field in the sheath region impacting the substrate surface and interfering with the growth of graphene, creating more defects.

Thus, the graphene quality is worse when it is closer to the plasma source. Precise control of the growth time and growth distance are necessary to avoid excessive defects in graphene.

Next, to investigate the effect of different growth temperatures on graphene quality, we conducted growth experiments at 500 °C, 400 °C, and 300 °C. The distance between the samples and the plasma source was divided into six groups, between 12 cm and 21 cm. As shown in Fig. 2d–f, the comparison between different growth temperatures reveals that higher temperatures yield higher-quality graphene. In Fig. 2d, at 500 °C the Raman spectrum shows the lowest I_D/I_G ratio 0.15. In contrast, Fig. 2e at 400 °C and Fig. 2f at 300 °C show increased I_D/I_G ratios, indicating more structural defects. At high temperatures (500 °C), the kinetic energy of carbon atoms is higher, which helps to overcome surface potential barriers, promotes grain growth, and reduces the formation of defects, hence improving graphene quality. As the temperature decreases to 400 °C and 300 °C, the activity of carbon atoms diminishes, leading to relatively poorer graphene crystallinity and more defects, such as single vacancies and multi-vacancies. Additionally, Fig. 2d–f, again, show that the quality of graphene is generally lower when the sample is closer to the plasma source.
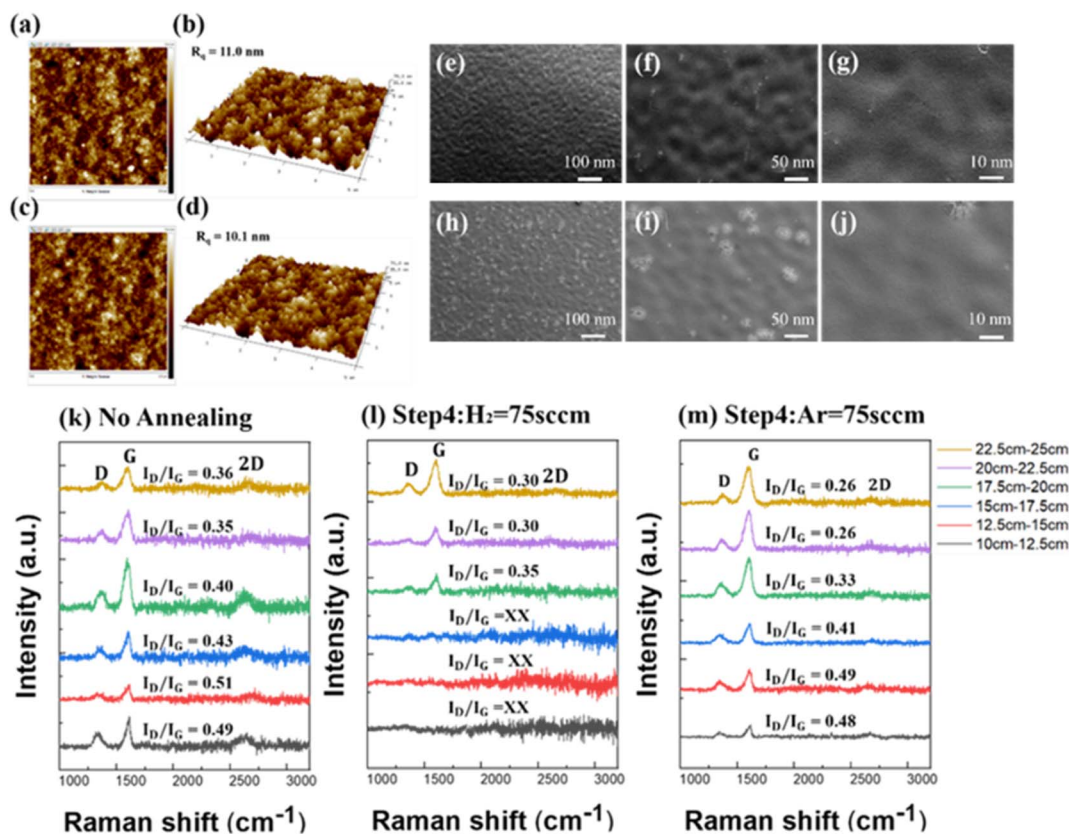
Fig. 3 The effect of the laser treatment and low-temperature annealing. (a–d) AFM images of graphene/copper foil samples. (a) and (b) are AFM and AFM-3D images without laser treatment, respectively. (c) and (d) are AFM and AFM-3D images with 30 W laser pretreatment, respectively. (e–j) SEM images of the copper foil before and after the laser treatment. (e–g) show surface images without laser treatment at magnifications of 100×, 500×, and 1000×, respectively. (h–j) are surface images with 30 W laser treatment at magnifications of 100×, 500×, and 1000×, respectively. (k–m) Comparison of Raman spectra for the samples grown at 400 °C with different annealing conditions. (k) No annealing. (l) Annealing with H$_2$ gas (75 sccm). (m) Annealing with Ar gas (75 sccm). The distance between the samples and the plasma source was divided into six groups, between 10 cm and 25 cm.

To improve the quality of graphene under the same growth temperature and time, the copper substrate can be pretreated by laser to remove copper oxide or surface particles. This treatment helps improve the adsorption and nucleation process of the carbon source on the substrate, effectively promoting high-quality graphene growth. Fig. 2g shows the laser pretreatment process flow for the copper foil and the growth timetable in this experiment. The copper foil is first placed in a CO_2 laser machine for laser pretreatment with different laser powers. After the N_2 gas purge, the copper foil is inserted into the PECVD chamber for graphene growth. Fig. 2h–j shows the effect of laser pretreatment on graphene growth at three different growth distances at 400 °C. In Fig. 2h, at a 12–15 cm distance from the plasma source, the copper substrate becomes smoother after 30 W laser treatment, which helps reduce nucleation density during the growth process, resulting in an I_D/I_G ratio of 0.41. However, the improvement between with and without laser treatment is limited because high-energy radicals and ions still interfere with graphene nucleation and growth by impacting the substrate at this short growth distance. In Fig. 2i, at a distance of 15–18 cm, as the laser pretreatment intensity increases, the surface oxides and particles on the substrate are reduced, lowering the defect peak. The I_D/I_G ratio decreases from 0.46 without laser treatment to 0.31 after 30 W laser treatment, which is a 33% improvement. In Fig. 2j, at a distance of 18–21 cm, the I_D/I_G ratio decreases from 0.43 without laser treatment to 0.27 with 30 W laser treatment, showing a 37% improvement. Overall, the Raman spectra show a strong and broad D band, revealing that the material is defective or nanocrystalline graphene rather than monolayer graphene. The weak and broadened 2D band confirms that the films are not monolayer or bilayer, but instead few-layer graphene. The presence of a clear G band indicates a preserved sp^2 lattice, while the large I_D/I_G suggests small crystalline domains. Among all conditions, the 30 W laser treatment sample after the 400 °C annealing step exhibits the lowest I_D/I_G ratio, the sharpest G peak, and the most discernible 2D feature, indicating the best overall graphene quality. The above laser pretreatment results suggest that the smoothness and cleanliness of the copper foil surface have a significant impact on graphene nucleation and growth. Laser treatment can improve the surface smoothness of the copper foil by localized heating and melting, lowering the nucleation density of graphene and promoting uniform graphene growth.

Fig. 3a–d are the atomic force microscopy (AFM) images showing the surface morphology before and after the laser treatment. (All AFM images here were processed with second-order differentiation.) Fig. 3a and b are the AFM and AFM-3D images of the copper foil before the laser pretreatment, respectively, while Fig. 3c and d are the AFM and AFM-3D images of the copper foil after the laser pretreatment, respectively. In Fig. 3a and b, the AFM images display noticeable protrusions (white regions), which are likely copper particles or copper oxide. These protrusions lead to uneven distribution of graphene nucleation sites, with defects during graphene growth often forming at these raised or recessed areas. After the laser pretreatment, the AFM images in Fig. 3c and d show that most

of the protrusions on the copper foil surface have been removed, and the surface undulations are significantly reduced. The surface root mean square roughness (R_q) decreased from 11.0 nm to 10.1 nm after the laser treatment. A smoother substrate surface provides a more uniform distribution of nucleation sites, thereby reducing the defect density in the graphene layers. This result is consistent with the observation in Fig. 2h–j.

Next, scanning electron microscopy (SEM) was used to investigate the changes in the copper foil surface before and after the laser pretreatment. Fig. 3e–g are SEM images of the copper foil surface before the laser pretreatment at magnifications of 100×, 500×, and 1000×, respectively. These images show noticeable white protrusions on the copper foil surface, which are speculated to be copper particles. Significant height differences are also observed on the copper foil surface, indicating unevenness. Fig. 3h–j are SEM images of the copper foil surface after the laser pretreatment at magnifications of 100×, 500×, and 1000×, respectively. These images show that the copper foil surface becomes smoother after the laser treatment, with the protruding copper particles being flattened by the laser, and the overall height differences are significantly reduced. Fig. 3e–j demonstrates that laser pretreatment effectively improves the smoothness of the copper foil and removes surface protrusions, which helps reduce nucleation density during graphene growth, hence improving the quality and continuity of the PECVD graphene film.

In the low-temperature annealing process, defects such as dislocations and vacancies can rearrange, reducing internal stress and improving the ductility of the graphene film. To further explore the annealing conditions in the step 4 of Fig. 1b, the samples were placed at distances of 10 to 25 cm from the plasma source and divided into six groups (Fig. 3k–m). The first group, closest to the plasma source, ranges from 10 to 12.5 cm, while the sixth group, the farthest, ranges from 22.5 to 25 cm. Different gas flows were used during the annealing process to investigate the impact on the quality of the resulting graphene film. Fig. 3k shows the Raman spectrum of graphene grown at 400 °C without annealing, while Fig. 3l shows the Raman spectrum of graphene grown at 400 °C with 75 sccm H_2 gas in the annealing process. In Fig. 3l, the black, red, and blue curves do not have distinct D and G peaks, while the samples represented by green, purple, and dark yellow curves show significant quality improvement compared to the non-annealed samples, with the lowest $I_D/I_G = 0.30$. This is because that, for the samples closer to the ventilation port (i.e., black, red, and blue curves), the impact of hydrogen flow is more severe, potentially causing hydrogenation reactions with the benzene (C_6H_6) carbon source, forming cyclohexane (C_6H_{12}) via the reaction $C_6H_6 + 3H_2 \rightarrow C_6H_{12}$. Excessive reactions between hydrogen atoms and the carbon source can deplete the carbon source, reducing the number of carbon atoms available for nucleation and thereby hindering graphene growth. The hydrogenation reaction may also lead to the formation of unwanted hydrocarbons on the substrate surface, affecting graphene nucleation and growth. Therefore, selecting the appropriate gas during annealing is crucial. Inert gases like argon can prevent carbon

(a)

Before Oxidation

Sample \\ Sheet Resistance	Copper foil	400 °C Graphene/Copper	Annealing at 400 °C Graphene/Copper	30W Laser Pretreatment + Annealing at 400 °C Graphene/Copper
Data 1	1.6105 Ω/□	0.7431 Ω/□	0.6613 Ω/□	0.5402 Ω/□
Data 2	1.6198 Ω/□	0.7315 Ω/□	0.6667 Ω/□	0.5503 Ω/□
Data 3	1.6571 Ω/□	0.7834 Ω/□	0.6412 Ω/□	0.5374 Ω/□
Data 4	1.6452 Ω/□	0.7312 Ω/□	0.6718 Ω/□	0.5363 Ω/□
Data 5	1.6963 Ω/□	0.7393 Ω/□	0.6343 Ω/□	0.5631 Ω/□
Average Sheet Resistance	1.6458 Ω/□	0.7457 Ω/□	0.6551 Ω/□	0.5455 Ω/□

After Oxidation

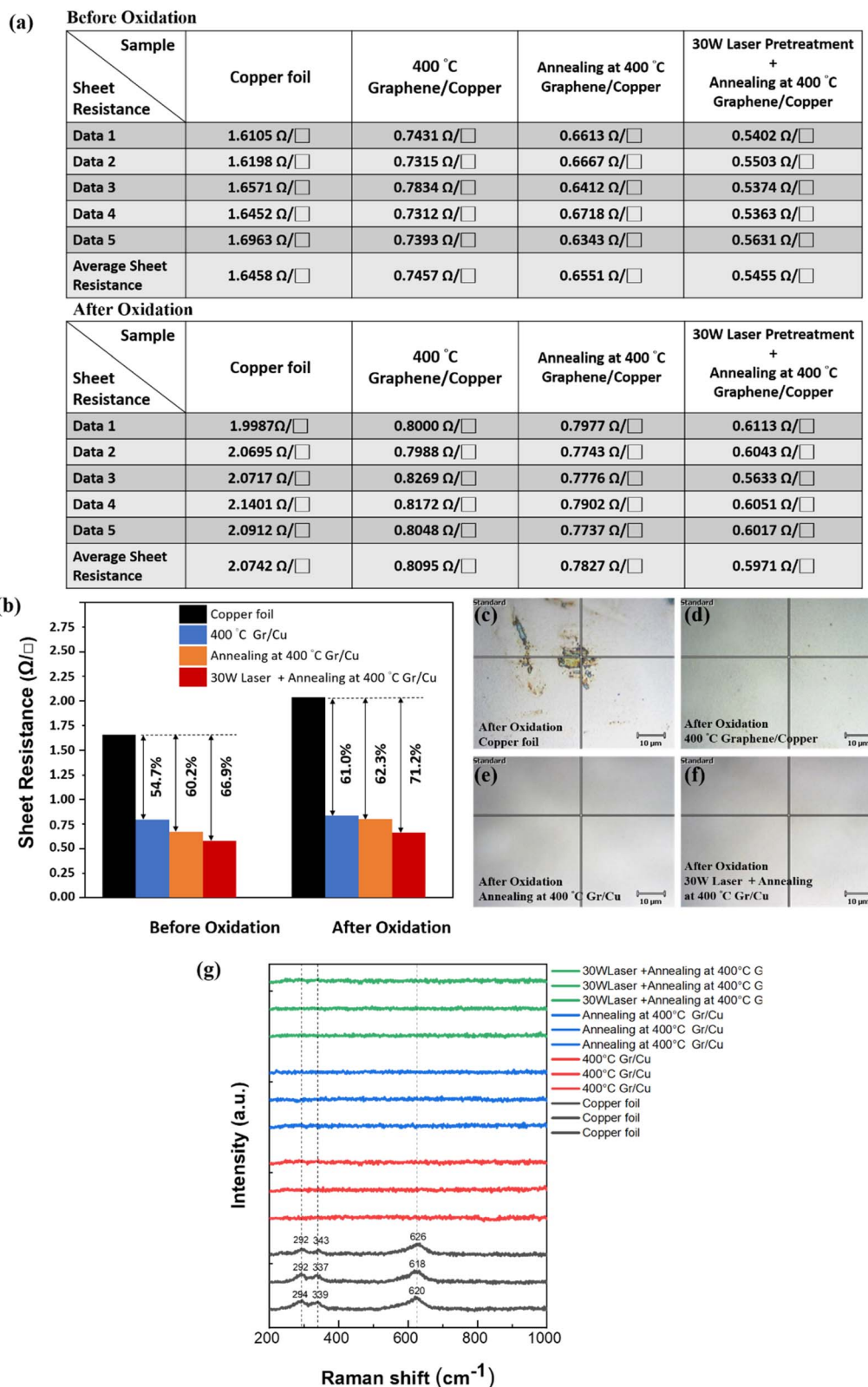| Sample \\ Sheet Resistance	Copper foil	400 °C Graphene/Copper	Annealing at 400 °C Graphene/Copper	30W Laser Pretreatment + Annealing at 400 °C Graphene/Copper
Data 1	1.9987 Ω/□	0.8000 Ω/□	0.7977 Ω/□	0.6113 Ω/□
Data 2	2.0695 Ω/□	0.7988 Ω/□	0.7743 Ω/□	0.6043 Ω/□
Data 3	2.0717 Ω/□	0.8269 Ω/□	0.7776 Ω/□	0.5633 Ω/□
Data 4	2.1401 Ω/□	0.8172 Ω/□	0.7902 Ω/□	0.6051 Ω/□
Data 5	2.0912 Ω/□	0.8048 Ω/□	0.7737 Ω/□	0.6017 Ω/□
Average Sheet Resistance	2.0742 Ω/□	0.8095 Ω/□	0.7827 Ω/□	0.5971 Ω/□

Fig. 4 Electrical properties and surface characteristics of graphene/copper foil in oxidation experiments. (a) Sheet resistance of graphene/copper foil structures with different treatments before and after oxidation. (b) Comparison of sheet resistance before and after oxidation. (c–f) OM images of copper foil and graphene/copper foil with different treatments after oxidation. (c) Pure copper foil after oxidation. (d) Graphene/copper foil after oxidation. (e) Graphene/copper foil with 400 °C annealing after oxidation. (f) Graphene/copper foil with the 30 W laser pretreatment and 400 °C annealing after oxidation. (g) Raman spectra of copper foil and graphene/copper foil with different treatments after oxidation. CuO peaks are observed in the Raman spectrum of oxidized pure copper foil.

source contamination or oxidation, thereby preserving the quality of graphene. In Fig. 3m, after introducing 75 sccm of Ar gas in the annealing process, the quality of samples shows a significant improvement compared to the samples in Fig. 3k and l. Especially at the optimal growth distance (*i.e.*, 22.5–25 cm), the I_D/I_G ratio of graphene reaches a minimum of 0.26, which is a 28% improvement compared to $I_D/I_G = 0.36$ of the non-annealed samples at the same distance. This indicates that during the low-temperature annealing stage, the introduction of a small amount of argon provides a uniform and inert thermal environment, allowing carbon atoms to deposit evenly on the substrate and aiding in the repair of defects in graphene, which ultimately improves the quality of the graphene. Moreover, Raman spectra collected from both the as-grown graphene/Cu samples and the graphene films after transfer to Si consistently showed no CuO vibration modes, indicating that the copper surface remained well protected from oxidation. This result also suggests good mechanical stability of the graphene layer, as the film maintained its integrity and protective function throughout growth, handling, and transfer without introducing defects that would expose the underlying copper to oxidation.

As the application of graphene in high-performance electronic and optoelectronic components continues to expand, further reducing the growth temperature to achieve more energy-efficient processes becomes increasingly important.[34–36] Our studies have confirmed the successful growth of high-quality graphene at 400 °C with the annealing treatment, which prompts us to explore the feasibility and advantages of an even lower growth and annealing temperature at 300 °C. However, samples grown and annealed at 300 °C (Fig. S8) did not give the same high-quality results as those at 400 °C. We speculated that insufficient kinetic energy for carbon atoms at 300 °C makes it difficult for graphene to coalesce

and nucleate during the dehydrogenation stage (see detailed discussion in SI).

3.2 Graphene electrical property analysis

In the electrical property analysis, a four-point probe was used to measure the sheet resistance of graphene/copper foil and pure copper foil under different process parameters. To validate the anti-oxidation properties of graphene, the samples were exposed to air at 100 °C in an oven for 4 hours to simulate oxidation conditions. The electrical resistances before and after oxidation were then compared using a four-point probe. Optical microscopy and Raman spectroscopy were also employed to examine the samples before and after oxidation.

Fig. 4a shows the changes in sheet resistance of different samples before and after oxidation, and the numerical values are reported exactly as recorded by the measurement instruments. Before oxidation, the surface of pure copper foil had an average sheet resistance of 1.6458 Ω/□. Graphene grown on copper foil at 400 °C reduced the average resistance from 1.6458 Ω/□ to 0.7457 Ω/□. The graphene grown after annealing treatment further reduced the average resistance to 0.6551 Ω/□. With 30 W CO_2 continuous laser pretreatment and annealing, the graphene exhibited the fewest defects (Fig. 3m, I_D/I_G = 0.26) and achieved the lowest average resistance of 0.5455 Ω/□. After 4 hours of oxidation at 100 °C in air, the pure copper foil became CuO, and the oxidation layer caused the inelastic scattering of electrons between graphene and copper, significantly increasing the average resistance from 1.6458 Ω/□ to 2.0742 Ω/□. In contrast, samples with graphene coating suppressed the formation of the oxidation layer, resulting in a smaller increase in sheet resistance. The average sheet resistance of the samples with graphene grown at 400 °C without annealing, graphene grown at 400 °C with annealing, and
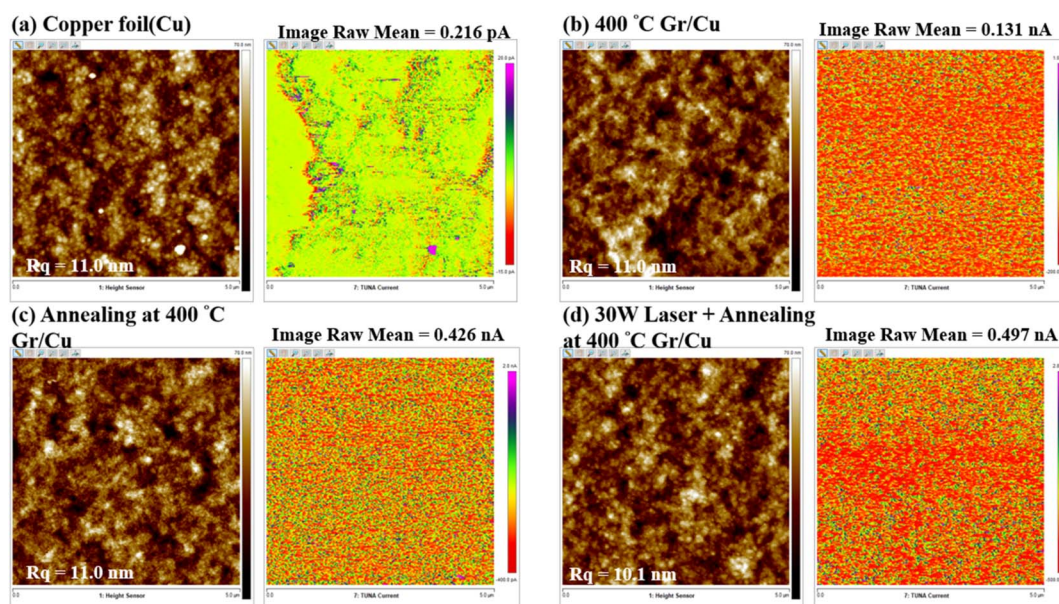

Fig. 5 The AFM images and the corresponding C-AFM images. (a) Pure copper foil, (b) graphene grown on copper foil at 400 °C, (c) graphene grown on copper foil after annealing at 400 °C, and (d) graphene grown on copper foil after the 30 W laser treatment and annealing at 400 °C.

graphene grown at 400 °C with 30 W laser pretreatment and annealing are 0.8095 Ω/□, 0.7827 Ω/□, and 0.5971 Ω/□, respectively.

As shown in Fig. 4b, the oxidation experiment indicates that the presence of graphene effectively reduces the sheet resistance and provides protection against oxidation. Before oxidation, the graphene grown with the laser treatment and annealing process showed the highest conductance, with a 66.9% improvement in sheet resistance compared to the pure copper foil. After the oxidation experiment, the sheet resistance of graphene grown with the laser treatment and annealing processes improved by 71.2% compared to oxidized copper foil. Fig. 4c–f show OM images of the pure copper foil, graphene grown at 400 °C, graphene with annealing at 400 °C, and graphene grown with 30 W laser pretreatment and annealing at 400 °C after the oxidation experiment, respectively. It can be seen that the pure copper foil (Fig. 4c) shows signs of oxidation on the surface. In contrast, the samples protected by graphene (Fig. 4d–f) show no significant oxidation on the surface. Raman spectroscopy analysis in the

range from 200 to 1000 cm^{-1} further confirms this result (Fig. 4g). Each sample was tested three times in different regions. The Raman spectra of oxidized pure copper foil display typical CuO peaks (288, 330, and 621 cm^{-1}), while the samples protected by graphene do not have these peaks, indicating that graphene can effectively prevent copper oxidation. In summary, through a comprehensive evaluation of electrical properties and surface characteristics, it is clear that graphene provides protection against oxidation for copper substrates, especially in graphene/copper foil samples with laser pretreatment and annealing, in which both oxidation resistance and electrical conductance are significantly improved.

The use of conductive atomic force microscopy (C-AFM) allows for direct visualization of changes in the current distribution on the graphene surface. Fig. 5a–d show the AFM images and the corresponding C-AFM images for pure copper foil, graphene grown on copper foil at 400 °C, graphene grown on copper foil with annealing at 400 °C, and graphene grown on copper foil with the 30 W laser treatment and annealing at 400 °
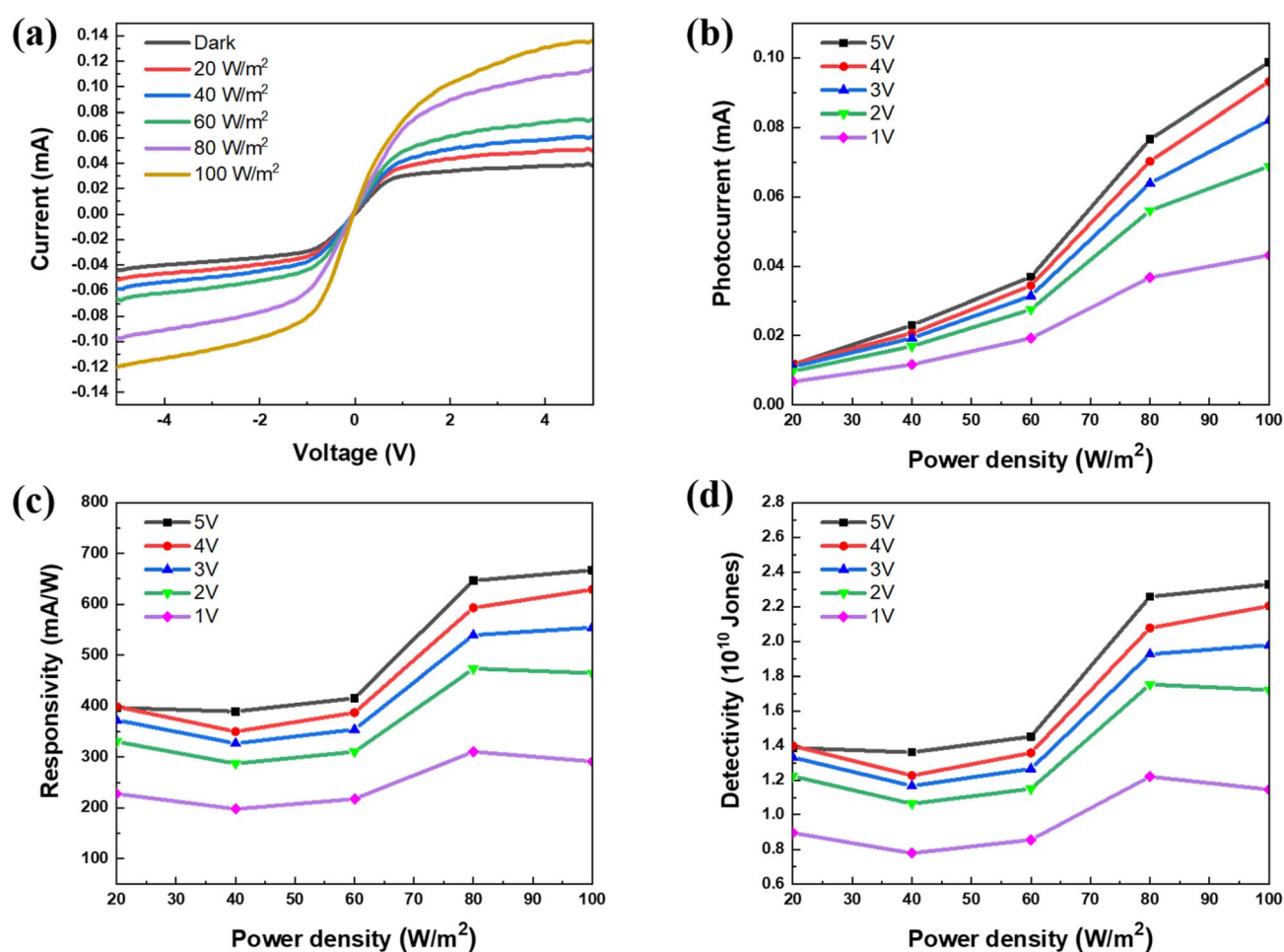

Fig. 6 The performance of the graphene/Si photodetector. (a) The current–voltage relations of graphene photodetector under different light intensities. (b) The relation between the photocurrent of the graphene photodetector and the incident light power density in the bias range from 1 V to 5 V. (c) The relation between the responsivity of the graphene photodetector and the incident light power density in the bias range from 1 V to 5 V. (d) The relation between the specific detectivity of the graphene photodetector and the incident light power density in the bias range from 1 V to 5 V.

C, respectively. By measuring the surface roughness through AFM, it can be determined that the R_q (root mean square roughness) for Fig. 5a–c is 11.0 nm. With the laser treatment (Fig. 5d), the R_q value decreases to 10.1 nm, showing an improvement in roughness by 8.2%.

As shown in the C-AFM images in Fig. 5a, the current distribution indicates that the image raw mean for pure copper foil is 0.216 pA. In Fig. 5b, after growing graphene on the copper foil at 400 °C, the Image Raw Mean increases to 0.131 nA. In Fig. 5c, the Image Raw Mean for graphene grown on copper foil after annealing at 400 °C is 0.426 nA. The best quality is observed in Fig. 5d, where the graphene grown after the 30 W laser treatment and annealing at 400 °C shows the highest image raw mean of 0.497 nA. This is about four times larger than the current in Fig. 5b. These results indicate that the laser treatment and annealing significantly improve the quality and electrical properties of the graphene/copper foil structure.

3.3 Graphene photodetector performance

The graphene with the highest quality ($I_D/I_G = 0.26$) in Fig. 3m was used to fabricate a photodetector. The current–voltage (I–V) characteristics of the graphene-based photodetector under different light intensities were investigated using halogen white light with powers of 20, 40, 60, 80, and 100 W m^{-2} as the illumination source. The effective illuminated area of the device is 0.0148 cm^2. The changes in the I–V curve from −5 V to 5 V under both dark and illuminated conditions were analyzed, as shown in Fig. 6a. First, it can be seen that the current is proportional to the voltage under both dark and illuminated conditions. Second, it demonstrates positive photoconductivity (PPC), *i.e.*, the photo-current increases with increasing light intensity. When the light intensity increased from 20 W m^{-2} to 100 W m^{-2}, the current significantly increased from 0.035 mA to 0.137 mA. Additionally, because graphene formed a uniform film after being transferred onto the silicon substrate, the current values for the forward bias and reverse bias conditions were nearly identical, resulting in a symmetrical current–voltage graph.

Fig. 6b shows the variation of the photocurrent of the graphene photodetector under different incident light power densities. In the bias range from 1 V to 5 V, the photocurrent increased as the incident light power density increased from 20 to 100 W m^{-2}. Particularly under a 5 V bias, the photocurrent rose from 0.01175 mA to 0.09871 mA, indicating that the device has good photocurrent response and stability.

Photodetector responsivity is a key indicator of the photoelectric conversion efficiency. The formula for calculating responsivity is shown in eqn (1), where R is the responsivity, the photocurrent I_{photo} is the difference between the illuminated current I_{Light} and the dark current I_{Dark} (*i.e.*, under no illumination), P_{photo} is the incident light power density, A is the effective area of the device under illumination, q is the absolute value of the elementary charge, h is the Planck's constant, v and λ are the frequency and wavelength of the incident light, respectively. The external quantum efficiency (EQE) is also taken into account. High responsivity means good photoelectric conversion efficiency and sensitivity.

$$R = \frac{I_{photo}}{P_{photo}A} = \frac{q}{hv} \times \text{EQE}(\lambda) = \frac{\lambda}{1240} \times \text{EQE}(\lambda) \quad (1)$$

Fig. 6c shows the responsivity of the graphene photodetector in this experiment. Under different biases (1 V to 5 V), the responsivity increased with the incident light power density. Especially under a 5 V bias, the responsivity reached a maximum of 666.95 mA W^{-1}, suggesting higher photoelectric conversion efficiencies at higher power densities. We note that the responsivity did not show a significant increase when the power density of the incident light increased from 80 W m^{-2} to 100 W m^{-2}. This is possibly due to the saturation of graphene's light absorption capability at high power densities, leading to an insignificant improvement in responsivity and even a slight decrease under the 1 V bias.[37,38]

The specific detectivity (D^*) is also an important parameter for evaluating the performance of photodetectors, which represents the minimum detectable signal of the device. The higher the D^* value, the better the detecting capability of the device. The definition of D^* is shown in eqn (2), where A is the effective illuminated area of the device, R is the responsivity, q is the absolute value of the elementary charge, and I_{dark} is the dark current of the device. The unit of specific detectivity is cmHz$^{1/2}$ W^{-1}, commonly expressed in Jones.

$$D^* = \frac{A^{0.5}R}{(2qI_{dark})^{0.5}} \quad (2)$$

Fig. 6d shows the specific detectivity of the graphene photodetector under different incident light power densities at biases ranging from 1 V to 5 V. As the applied bias increased, the overall detectivity of the device increased accordingly. Under a 5 V bias, D^* reached a maximum value of 2.32×10^{10} Jones at 100 W m^{-2}. The power density dependence of D^* is similar to that of the responsivity. These results demonstrate that the graphene photodetector has a good photoelectric conversion performance under different incident light power densities, and both the responsivity and specific detectivity of the device significantly improve as the applied bias or incident light intensity increases.

The switching response of a photodetector is another important indicator for evaluating its performance. To check the switching response, a halogen white light source with light intensities ranging from 60 to 100 W m^{-2} was used to conduct time-dependent photocurrent response measurements. The light was turned on and off every 30 seconds for five cycles. Fig. 7a shows the time-dependent photocurrent response of the graphene photodetector at a 5 V bias under different light intensities. The photocurrent of the device responded quickly to the switching of light under all illumination intensities. As the light power density increased, the photocurrent also increased, consistent with the results in Fig. 6b. Additionally, during multiple on-off cycles, the photocurrent consistently returned to its initial value, demonstrating that the graphene photodetector maintained good stability and reproducibility under repetitive operations.
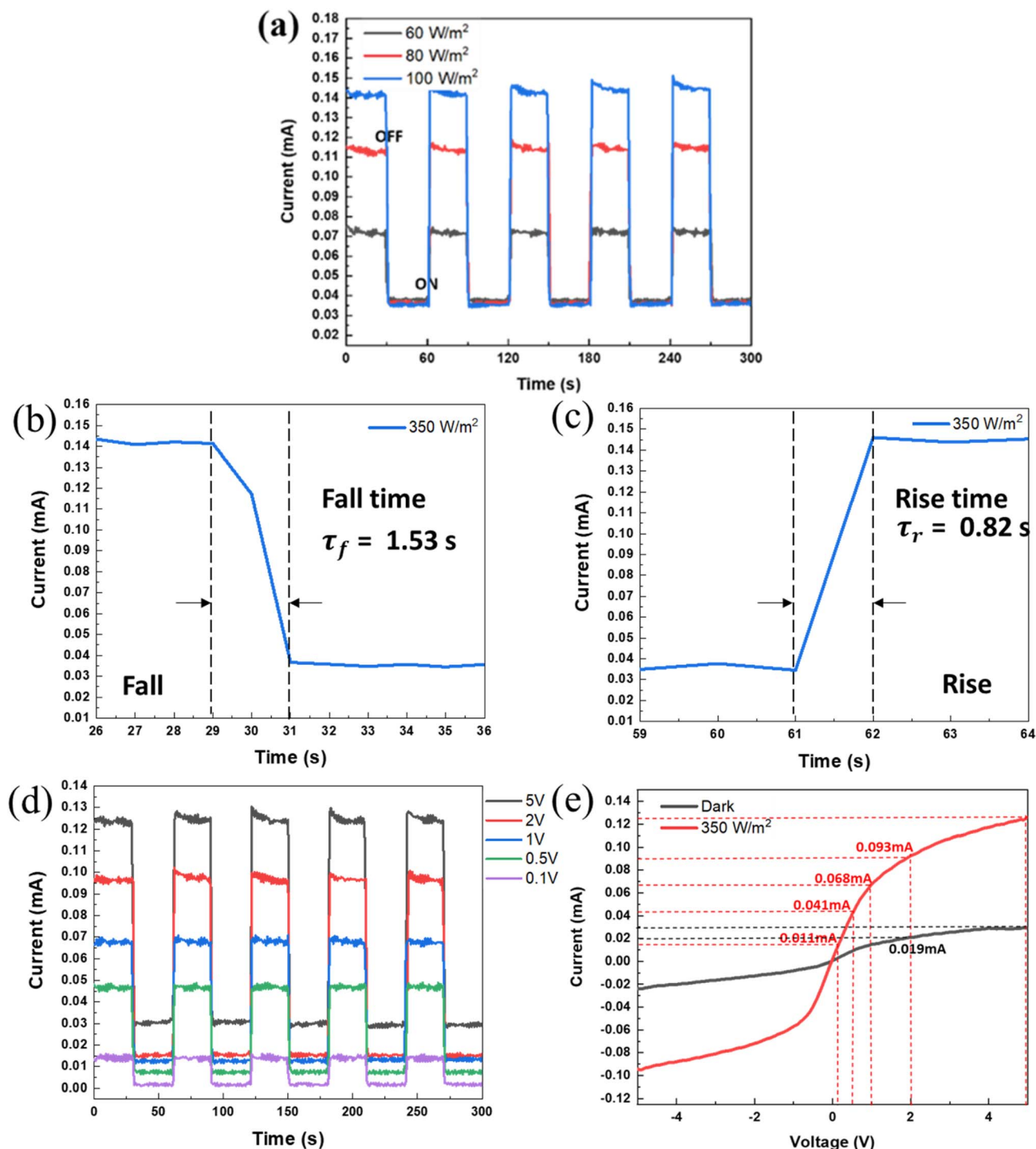
Fig. 7 The switching response of the graphene/Si photodetector. (a) The photoresponse of the graphene photodetector under different light intensities at a 5 V bias. The photocurrent responded quickly to the switching of light and showed good reproducibility under repetitive operations. (b and c) The (b) rise and (c) fall times of the photodetector under the illumination of 100 W m^{-2} white light at a bias of 5 V. (d and e) The photoresponse of the graphene photodetector under different biases and an illumination of 100 W m^{-2}. (d) The excellent stability and reproducibility of the graphene photodetector under repetitive switching operations at biases ranging from 5 V to 0.1 V. (e) The photodetector was able to detect a significant photocurrent of 0.011 mA even at a low working voltage of 0.1 V.

To study in more detail the response speed of the device during signal switching, the rise time and fall time of the photodetector were calculated. The rise time is defined as the time required for the current to increase from 10% to 90% of its maximum value after illumination, while the fall time is the time required for the current to decrease from 90% to 10% after the light is turned off. In this experiment, the rise and fall times of the photodetector were measured under the illumination of

a halogen white light source at an intensity of 100 W m^{-2} and a bias of 5 V. Fig. 7b and c show the rise time $\tau_r = 0.82$ seconds and fall time $\tau_f = 1.53$ seconds, respectively. The high response speed enables it to react quickly to the change in light source, making this photodetector suitable for applications that require rapid response.

We also investigated the switching response characteristics of the graphene photodetector under the illumination of 100 W m^{-2} light with different bias conditions, aiming to test the device's switching response capability in low-voltage power-saving modes and assess its stability during multiple on-off cycles. Fig. 7d shows the switching response at biases ranging from 5 V to 0.1 V during multiple on-off cycles. The photocurrent can quickly return to the initial value even at a low working voltage of 0.1 V under repetitive operations, indicating its good stability and reproducibility. In Fig. 7e, the device exhibits the best photocurrent response (0.126 mA) under a 5 V bias, suggesting that the photodetector is more effective in generating and collecting photogenerated carriers at higher biases. Nevertheless, under the low bias condition (0.1 V), the device was still able to detect a significant photocurrent of 0.011 mA, implying that this device has a sensitive photodetection capability even at low working voltages, which makes it highly promising for future energy-efficient applications.

4 Conclusions

This study investigates the quality of graphene under different growth and processing parameters, and its performance as a photodetector. Using plasma-enhanced chemical vapor deposition (PECVD), graphene with excellent quality was successfully grown at a low temperature (400 °C), offering significant advantages over the high-temperature environment required by traditional CVD. The laser pretreatment on the copper foil substrate and the low-temperature annealing process significantly improved the quality of graphene grown. High-quality graphene with a Raman I_D/I_G ratio of 0.26 was obtained. The graphene layer substantially increased the oxidation resistance and the electrical conductance of graphene/copper composite structures. A photodetector based on the as-grown graphene was then fabricated, and its performance was evaluated under different bias and illumination conditions. Under a 5 V bias and 100 W m^{-2} halogen lamp illumination, the photodetector achieved a responsivity of 666.95 mA W^{-1} and a detectivity of 2.32×10^{10} Jones. Moreover, the excellent stability under repetitive operation and good switching characteristics even at a low working voltage (0.1 V) imply great potential for applications in energy-efficient systems. More work on optimizing the PECVD processing parameters, exploring different carbon source materials, and expanding the scope of potential applications will be conducted to facilitate the commercialization of this low-temperature-synthesized high-quality graphene.

Conflicts of interest

The authors declare no conflict of interest.

Data availability

The data supporting this article have been included as part of the supplementary information (SI). Supplementary information is available. See DOI: https://doi.org/10.1039/d5na00799b.

Acknowledgements

References

1 R. R. Nair, P. Blake, A. N. Grigorenko, K. S. Novoselov, T. J. Booth, T. Stauber and A. K. Geim, *Science*, 2008, **320**, 1308.

2 A. H. Castro Neto, F. Guinea, N. M. Peres, K. S. Novoselov and A. K. Geim, *Rev. Mod. Phys.*, 2009, **81**, 109.

3 S. Wang, P. K. Ang, Z. Wang, A. L. L. Tang, J. T. Thong and K. P. Loh, *Nano Lett.*, 2010, **10**, 92–98.

4 K. Jayaramulu, M. Horn, A. Schneemann, H. Saini, A. Bakandritsos, V. Ranc and R. A. Fischer, *Adv. Mater.*, 2021, **33**, 2004560.

5 M. J. Nine, M. A. Cole, D. N. Tran and D. Losic, *J. Mater. Chem. A*, 2015, **3**, 12580–12602.

6 D. Berman, S. A. Deshmukh, S. K. Sankaranarayanan, A. Erdemir and A. V. Sumant, *Adv. Funct. Mater.*, 2014, **24**, 6640–6646.

7 D. Prasai, J. C. Tuberquia, R. R. Harl, G. K. Jennings and K. I. Bolotin, *ACS Nano*, 2012, **6**, 1102.

8 S. Chen, L. Brown, M. Levendorf, W. Cai, S. Y. Ju, J. Edgeworth and R. S. Ruoff, *ACS Nano*, 2011, **5**, 1321.

9 Q. Yu, J. Lian, S. Siripongleert, H. Li, Y. P. Chen and S. S. Pei, *Appl. Phys. Lett.*, 2008, **93**, 111116.

10 L. G. De Arco, Y. Zhang, A. Kumar and C. Zhou, *IEEE Trans. Nanotechnol.*, 2009, **8**, 135.

11 X. Li, W. Cai, J. An, S. Kim, J. Nah, D. Yang and R. S. Ruoff, *Science*, 2009, **324**, 1312.

12 C. Mattevi, H. Kim and M. Chhowalla, *J. Mater. Chem.*, 2011, **21**, 3324.

13 X. Chen, L. Zhang and S. Chen, *Synth. Met.*, 2015, **210**, 95.

14 G. Deokar, J. Avila, I. Razado-Colambo, J. L. Codron, C. Boyaval, E. Galopin and D. Vignaud, *Carbon*, 2015, **89**, 82.

15 L. Lin, B. Deng, J. Sun, H. Peng and Z. Liu, *Chem. Rev.*, 2018, **118**, 9281.

16 B. Zhang, W. H. Lee, R. Piner, I. Kholmanov, Y. Wu, H. Li and R. S. Ruoff, *ACS Nano*, 2012, **6**, 2471.

17 J. Kim, H. Sakakita and H. Itagaki, *Nano Lett.*, 2019, **19**, 739.

18 T. Yamada, M. Ishihara and M. Hasegawa, *Appl. Phys. Express*, 2013, **6**, 115102.

19 G. Kalita, K. Wakita and M. Umeno, *RSC Adv.*, 2012, **2**, 2815.

20 L. W. Jang, L. Zhang, M. Menghini, H. Cho, J. Y. Hwang, D. I. Son and J. W. Seo, *Carbon*, 2018, **139**, 666.

21 B. Lee and W. Li, *Mater. Lett.*, 2020, **273**, 127875.

22 H. Kashani, C. Kim, C. Rudolf, F. K. Perkins, E. R. Cleveland and W. Kang, *Adv. Mater.*, 2021, **33**, 2104208.

23 Z. Gao, T. Zuo, M. Wang, L. Zhang, B. Da, Y. Ru and L. Xiao, *Carbon*, 2022, **186**, 303.

24 S. J. Kim, D. H. Shin, Y. S. Choi, H. Rho, M. Park, B. J. Moon and S. Bae, *ACS Nano*, 2018, **12**, 2803.

25 Y. Ahn, Y. Jeong, D. Lee and Y. Lee, *ACS Nano*, 2015, **9**, 3125.

26 S. Chaitoglou and E. Bertran, *J. Mater. Sci.*, 2017, **52**, 8348.

27 A. Dathbun and S. Chaisitsak, *IEEE Int. Conf. Nano/Micro Eng. Mol. Syst.*, 2013, 1018–1021.

28 L. Zheng, X. Cheng, P. Ye, L. Shen, Q. Wang, D. Zhang and Y. Yu, *RSC Adv.*, 2018, **8**, 1477–1480.

29 M. J. Josline, E. T. Kim and J. H. Lee, *Appl. Sci. Converg. Technol.*, 2022, **31**, 63–70.

30 Y. Jin, B. Hu, Z. Wei, Z. Luo, D. Wei, Y. Xi and Y. Liu, *J. Mater. Chem. A*, 2014, **2**, 16208.

31 A. Alnuaimi, I. Almansouri, I. Saadat and A. Nayfeh, *RSC Adv.*, 2017, **7**, 51951.

32 M. D. Bhatt, H. Kim and G. Kim, *RSC Adv.*, 2022, **12**, 21520.

33 C. Kang, D. H. Jung, J. E. Nam and J. S. Lee, *J. Nanosci. Nanotechnol.*, 2014, **14**, 9169–9173.

34 X. Zhang, T. Wu, Q. Jiang, H. Wang, H. Zhu, Z. Chen and X. Xie, *Small*, 2019, **15**, 1805395.

35 Y. I. Zhang, L. Zhang and C. Zhou, *Acc. Chem. Res.*, 2013, **46**, 2329–2339.

36 F. Qian, J. Deng, Y. Dong, C. Xu, L. Hu, G. Fu and J. Sun, *ACS Appl. Mater. Interfaces*, 2022, **14**, 53174–53182.

37 F. Luo, M. Zhu, H. Sun, W. Luo, G. Peng, Z. Zhu and S. Qin, *AIP Adv.*, 2018, **8**, 115003.

38 Y. Wang, Z. Zhang, Y. Zhang, M. Feng, H. K. Tsang, in *2019 Asia Commun. Photonics Conf. (ACP)*, IEEE, 2019, 1–3.